



HAL
open science

A systematic numerical study of the tidal instability in a rotating triaxial ellipsoid

D. Cébron, M. Le Bars, J. Leontini, P. Maubert, P. Le Gal

► To cite this version:

D. Cébron, M. Le Bars, J. Leontini, P. Maubert, P. Le Gal. A systematic numerical study of the tidal instability in a rotating triaxial ellipsoid. *Physics of the Earth and Planetary Interiors*, 2010, 182 (1-2), pp.119. 10.1016/j.pepi.2010.07.003 . hal-00675798

HAL Id: hal-00675798

<https://hal.science/hal-00675798>

Submitted on 2 Mar 2012

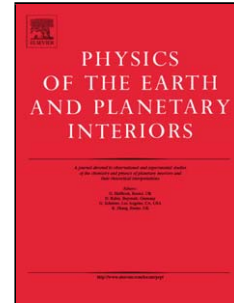
HAL is a multi-disciplinary open access archive for the deposit and dissemination of scientific research documents, whether they are published or not. The documents may come from teaching and research institutions in France or abroad, or from public or private research centers.

L'archive ouverte pluridisciplinaire **HAL**, est destinée au dépôt et à la diffusion de documents scientifiques de niveau recherche, publiés ou non, émanant des établissements d'enseignement et de recherche français ou étrangers, des laboratoires publics ou privés.

Accepted Manuscript

Title: A systematic numerical study of the tidal instability in a rotating triaxial ellipsoid

Authors: D. Cébron, M. Le Bars, J. Leontini, P. Maubert, P. Le Gal



PII: S0031-9201(10)00145-7
DOI: doi:10.1016/j.pepi.2010.07.003
Reference: PEPI 5310

To appear in: *Physics of the Earth and Planetary Interiors*

Received date: 30-10-2009
Revised date: 6-7-2010
Accepted date: 7-7-2010

Please cite this article as: Cébron, D., Le Bars, M., Leontini, J., Maubert, P., Le Gal, P., A systematic numerical study of the tidal instability in a rotating triaxial ellipsoid, *Physics of the Earth and Planetary Interiors* (2010), doi:10.1016/j.pepi.2010.07.003

This is a PDF file of an unedited manuscript that has been accepted for publication. As a service to our customers we are providing this early version of the manuscript. The manuscript will undergo copyediting, typesetting, and review of the resulting proof before it is published in its final form. Please note that during the production process errors may be discovered which could affect the content, and all legal disclaimers that apply to the journal pertain.

A systematic numerical study of the tidal instability in a rotating triaxial ellipsoid

D. Cébron^{a,*}, M. Le Bars^a, J. Leontini^b, P. Maubert^a, P. Le Gal^a

^a*Institut de Recherche sur les Phénomènes Hors Equilibre, UMR 6594, CNRS et Aix-Marseille Universités, 49 rue F. Joliot-Curie, BP146, 13384 Marseille, France.*

^b*Department of Mechanical and Aerospace Engineering, Monash University, Clayton Campus Victoria 3800, Australia*

Abstract

The full non-linear evolution of the tidal instability is studied numerically in an ellipsoidal fluid domain relevant for planetary cores applications. Our numerical model, based on a finite element method, is first validated by reproducing some known analytical results. This model is then used to address open questions that were up to now inaccessible using theoretical and experimental approaches. Growth rates and mode selection of the instability are systematically studied as a function of the aspect ratio of the ellipsoid and as a function of the inclination of the rotation axis compared to the deformation plane. We also quantify the saturation amplitude of the flow driven by the instability and calculate the viscous dissipation that it causes. This tidal dissipation can be of major importance for some geophysical situations and we thus derive general scaling laws which are applied to typical planetary cores.

Keywords: tides, tidal/elliptical instability, planetary cores, finite element

*corresponding author

Email address: `cebron@irphe.univ-mrs.fr` (D. Cébron)

numerical simulations

1 **1. Introduction**

2 Tides are large scale deformations induced by gravitational interactions
3 that affect all the layers of a given planet or star. They play an important
4 role in geo- and astrophysics and so, many studies are devoted to this subject.
5 Their most obvious phenomena are of course the oceanic flows on Earth, but
6 tides are also responsible for the intense volcanism on Io for instance. In stars
7 but also in liquid planetary cores, tidal forcing induces an elliptical deforma-
8 tion of the rotating streamlines that may excite a parametric resonance of
9 inertial waves called the elliptical or tidal instability. This instability could,
10 for instance, be responsible for the surprising magnetic field in Io (Kerswell
11 and Malkus, 1998; Lacaze et al., 2006; Herreman et al., 2009) and for fluc-
12 tuations in the Earth's magnetic field on a typical timescale of 10,000 years
13 (Aldridge et al., 1997). It may also have a significant influence on the orbital
14 evolution of binary stars (Rieutord, 2003) and moon-planet systems (Le Bars
15 et al., 2010).

16 As described in the review of Kerswell (2002), the elliptical instability is
17 a three-dimensional instability which may grow as soon as a rotating fluid
18 possesses elliptical streamlines. As previously stated, it is due to a triadic
19 parametric resonance between two inertial waves of the rotating fluid (Kelvin,
20 1880) and the underlying strain field responsible for the elliptic deformation
21 (Bayly, 1986; Waleffe, 1990). Such an instability has been found in many
22 different contexts, including those where the strain field is due to vortex in-
23 teractions or to elliptically deformed boundaries. It has thus been the focus

24 of numerous theoretical and experimental studies, devoted to the dynamics
25 of two-dimensional turbulent flows (e.g. Widnall et al. (1974); Moore and
26 Saffman (1975) or Haj-Hariri and Homsy (1997) for a viscoelastic fluid), to
27 the stability of wakes (Leweke and Williamson, 1998a), to the dynamics of
28 vortex pairs (Leweke and Williamson, 1998b; Le Dizès and Laporte, 2002; Me-
29 unier et al., 2002), and to the flow inside deformed rotating cylinders (Gledzer
30 et al., 1975; Malkus, 1989; Eloy et al., 2000, 2003), ellipsoids (Gledzer and
31 Ponomarev, 1977; Kerswell, 1994; Lacaze et al., 2004) and shells (Aldridge
32 et al., 1997; Seyed-Mahmoud et al., 2004; Lacaze et al., 2005). More recently,
33 magnetohydrodynamical effects of the elliptical instability have been inves-
34 tigated, with applications in MHD turbulence (Thess and Zikanov, 2007) or
35 in induction processes in planets (Lacaze et al., 2006; Herreman et al., 2009).

36 From a numerical point of view, most studies have been devoted to the
37 dynamics of deformed two-dimensional vortices in three-dimensional domains
38 (e.g. Lundgren and Mansour, 1995; Sipp and Jacquin, 1998; Lacaze et al.,
39 2007; Roy et al., 2007). For instance, the seminal paper of Pierrehumbert
40 (1986) considered the growth of a perturbation on the planar velocity field as-
41 sociated with an elliptical vortex inside a box with zero normal-flow boundary
42 conditions, assuming periodicity in the axial direction; the linear eigenvalue
43 problem was then solved by spectral methods, and the growth rate of the
44 elliptical instability was found. Numerical studies in rotating containers are
45 less numerous. Mason and Kerswell (1999) used a non-orthogonal elliptico-
46 polar coordinate system in order to solve the flow in an elliptically deformed
47 cylinder by spectral methods; the non-linear temporal evolution of two dif-
48 ferent modes of the elliptical instability was calculated with no-slip boundary

49 conditions on the sidewalls and stress-free conditions on the top and the bot-
50 tom of the cylinder. Seyed-Mahmoud et al. (2000) determined numerically
51 the frequencies and the growth rates of the instability in both ellipsoid and
52 ellipsoidal shell geometries using a linear Galerkin method, projecting the
53 flow on a selected number of inertial waves. Finally, Shangli et al. (2007)
54 studied the stability of self-gravitating compressible ellipsoidal fluid configu-
55 rations and pointed out the occurrence of the elliptical instability. However,
56 to the best of our knowledge, the full non-linear evolution of the tidal in-
57 stability in an ellipsoidal geometry has not yet been simulated numerically.
58 This is the purpose of the present work, which aims at completing our pre-
59 vious theoretical and experimental investigations (Lacaze et al., 2004, 2006;
60 Herreman et al., 2009; Le Bars et al., 2010) in accessing global quantities of
61 fundamental importance for planetary applications.

62 In this paper, we focus on hydrodynamics only, leaving thermal and mag-
63 netic field interactions with the tidal instability for further investigations (e.g.
64 Cébron et al., 2010a). In section 2, the system and the numerical method
65 are presented. The numerical model is validated by comparison with the
66 theoretical results found in the literature, regarding the flow in a rotating
67 sphere submitted to a small and fixed elliptical deformation. In section 3,
68 we then study the influence of three additional complications of fundamental
69 importance for geophysical applications: (i) the influence of the length of the
70 ellipsoid along its rotation axis compared to the mean equatorial radius (i.e.
71 the body oblateness in geophysical terms), (ii) the influence of a background
72 rotation, corresponding to the orbital motion of the companion body respon-
73 sible for the tidal deformation, and (iii) the influence of the inclination of

74 the rotation axis compared to the deformation plane (i.e. the obliquity). In
 75 section 4, we quantify systematically two large-scale quantities relevant for
 76 planetary applications, namely (i) the amplitude of the instability at satura-
 77 tion, and (ii) the power dissipated by the instability. General laws in terms
 78 of dimensionless numbers are derived and applied to typical planetary cores
 79 in section 5.

80 2. Numerical model and its validation

81 2.1. Definition of the system and description of the numerical method

82 The present study takes place in direct continuity of our experimental
 83 studies of the elliptical instability in a deformed spheroid (Lacaze et al.,
 84 2004, 2006; Herreman et al., 2009; Le Bars et al., 2010). In these experi-
 85 ments, a hollow sphere of radius R , molded in a silicone cylinder, is filled
 86 with liquid and set in rotation at a constant angular velocity Ω about its
 87 axis (Oz), while it is slightly compressed by a quantity s along the axis
 88 (Ox), perpendicular to the rotation axis. The geometry is then a triaxial
 89 ellipsoid of axes $(a, b, c) = (R - s, R + s, R)$, with an equatorial ellipticity
 90 $\varepsilon = \frac{b^2 - a^2}{a^2 + b^2}$ and a constant tangential velocity along the deformed boundaries,
 91 equal to ΩR at the equator. Such a configuration is a model for a liquid
 92 planetary core with no solid inner core (e.g. like the jovian moon Io or the
 93 early Earth), surrounded by a deformable mantle with a constant tangential
 94 velocity. Similarly, our numerical model studies the rotating flow inside an
 95 ellipsoid of axes (a, b, c) related to the frame (Ox, Oy, Oz) , with a constant
 96 tangential velocity all along the boundary in each plane perpendicular to the
 97 rotation vector Ω (see the sketch in figure 1). In order to extend our previous

98 experimental study, the length c of the ellipsoid can be chosen independently
 99 of the other lengths a and b (with $b > a$). Moreover, the rotation axis of the
 100 ellipsoid can be inclined compared to the c -axis. Note however that in this
 101 paper, unless otherwise specified, we choose c equal to the mean equatorial
 102 radius $R_{eq} = (a + b)/2$ and a rotation axis along (Oz) , as in the experimental
 103 setup. In all simulations, the fluid is initially at rest and we suddenly impose
 104 at time $t = 0$ a constant angular rate Ω such that the tangential velocity
 105 along the deformed boundaries in each plane perpendicular to the rotation
 106 axis, is equal to $\Omega \frac{a'+b'}{2}$, where a' and b' are the axes of the elliptic bound-
 107 ary in this plane. In the following, results are non-dimensionalised using the
 108 mean equatorial radius R_{eq} as the length scale and Ω^{-1} as the time scale.
 109 Then five dimensionless numbers are used to fully describe the system: the
 110 Ekman number $E = \frac{\nu}{\Omega R_{eq}^2}$, where ν is the kinematic viscosity of the fluid,
 111 the ellipticity $\varepsilon = \frac{b^2 - a^2}{a^2 + b^2}$ of the elliptical deformation, the aspect ratio c/b
 112 which quantifies the oblateness of the ellipsoid, and finally the inclination θ
 113 and declination ϕ of the rotation axis. The problem numerically solved is
 114 then described by the following system of dimensionless equations:

$$\frac{\partial \mathbf{u}}{\partial t} + \mathbf{u} \cdot \nabla \mathbf{u} = -\nabla p + E \Delta \mathbf{u} - 2 \boldsymbol{\Omega}_c^* \times \mathbf{u}, \quad (1)$$

$$\nabla \cdot \mathbf{u} = 0. \quad (2)$$

116 where the no-slip boundary conditions are used for the fluid. Note that we
 117 work in the reference frame where the ellipsoidal shape is at rest, which is the
 118 inertial frame of reference in most of the paper. The Coriolis force $-2 \boldsymbol{\Omega}_c^* \times \mathbf{u}$
 119 is only used in section 3.2 where the whole triaxial ellipsoid is submitted to
 120 a global rotation at $\Omega_c^* \mathbf{e}_z$.

121 Usually, numerical studies of planetary cores benefit from their spherical
 122 geometry to use fast and precise spectral methods. In our case however,
 123 there is no simple symmetry. Our computations are thus performed with
 124 a standard finite element method widely used in engineering studies, which
 125 allows to deal with complex geometries, such as our triaxial ellipsoid, and
 126 to simply impose the boundary conditions. Note that a very efficient finite
 127 element method was recently introduced by Chan et al. (2010), but it is
 128 up to now restricted to spheroidal geometries ($a = b$). Using a commercial
 129 software¹, an unstructured mesh with tetrahedral elements was created. The
 130 mesh element type employed is the standard Lagrange element $P1 - P2$,
 131 which is linear for the pressure field but quadratic for the velocity field. Note
 132 that no stabilization techniques have been used in this work. We use the so-
 133 called Implicit Differential-Algebraic solver (IDA solver), based on backward
 134 differencing formulas (Hindmarsh et al., 2005). At each time step the system
 135 is solved with the sparse direct linear solver PARDISO².

136 The elliptical instability induces a three-dimensional destabilization of the
 137 initial two-dimensional elliptical streamlines. To study its global properties,
 138 it thus seems natural to introduce the mean value of the vertical velocity
 139 $W = \frac{1}{V} \iiint_V |w| \, d\tau$, with w the dimensionless vertical velocity and V the
 140 volume of the ellipsoid. The typical evolution of W as a function of time is
 141 shown in figure 2 (a) for $E = 1/500$ and $\varepsilon = 0.317$. At $t = 0$, the fluid is at
 142 rest in the ellipsoid, and the no-slip condition at the boundary proceeds to
 143 set the fluid in rotation. The first peak in W , just after $t = 0$, is due to the

¹COMSOL Multiphysics®

²www.pardiso-project.org

144 Ekman pumping which appears during the spin-up stage, which typically
 145 takes place over the Ekman time $t_E = E^{-1/2} \Omega^{-1}$, much faster than the
 146 viscous time scale $t_v = R_{eq}^2/\nu = E^{-1} \Omega^{-1}$ (Benton and Clark, 1974). For
 147 instance, in the case shown on figure 2 (a), the dimensionless Ekman time
 148 gives $\Omega t_E \approx 22$, which agrees with the numerical results. After this initial
 149 stage, the fluid is essentially in solid body rotation. From this state, the
 150 exponential growth of the instability can be seen, before an overshoot and
 151 a stationary saturation. Having defined the growth rate σ of the elliptical
 152 instability as the time constant of the exponential growth, a convergence
 153 study on this growth rate is given in the figure 2 (b). The number of degrees
 154 of freedom (DoF) used in most of the simulations of this work ranges between
 155 $4 \cdot 10^4$ DoF and $7 \cdot 10^4$ DoF, depending on the ellipticity and the Ekman
 156 number, in order to reach a compromise between a good convergence (see
 157 figure 2 (b)) and a reasonable CPU time.

158 2.2. Validation of our numerical simulations

159 A first visual validation is done on the shape of the flow in comparing the
 160 experimental visualisation on figure 3 (a) with the numerical simulation on
 161 figure 3 (b). As can be seen, we recover the classical S-shape of the spin-over
 162 mode, which induces an additional solid body rotation of the fluid around the
 163 axis of maximum strain, i.e. perpendicular to the imposed rotation axis (Oz)
 164 and at an angle of about 45° compared to the deformation axis (Ox) (Lacaze
 165 et al., 2004). In order to quantitatively validate the numerical model, the
 166 evolution of the growth rate of the instability is compared in figure 4 to the

167 linear theory given in Lacaze et al. (2004) for small ellipticities :

$$\frac{\sigma}{\varepsilon} = \frac{1}{2} - K \frac{\sqrt{E}}{\varepsilon}, \quad (3)$$

168 where K is a constant equal to $K = 2.62$ in the limit of small ε (Hollerbach
169 and Kerswell (1995); Lacaze et al. (2004)). Note that the second term on
170 the right hand side of the equation 3 corresponds to the viscous damping of
171 the growth rate due to the presence of Ekman layers near boundaries (see
172 Kudlick, 1966; Hollerbach and Kerswell, 1995). The expression (3) allows to
173 define a critical Ekman number for the onset of the instability equal to

$$E_c = \left(\frac{\varepsilon}{2K} \right)^2. \quad (4)$$

174 Close to the threshold, the numerical results closely follow the linear analysis,
175 for values of ellipticity as large as $\varepsilon \approx 0.5$. Note in particular that all curves
176 for various (ε, E) superimpose providing that σ/ε is expressed as a function of
177 \sqrt{E}/ε . This is especially interesting in order to apply our results to planets,
178 whose very small E are not directly accessible by our numerical tool, but can
179 be compensated for by large ε in simulations.

180 Finally, for very large ellipticities ($\varepsilon > 0.5$), figure 4 shows that the growth
181 rate decreases toward zero. The elliptical instability finally disappears for
182 ellipticities greater than a critical value which depends on the Ekman number.
183 The position of the maximum for the variation of σ with the ellipticity is
184 around $\varepsilon = 0.5$, whatever the Ekman number is. This indicates that the
185 decrease is probably due to geometrical effects related to the large value of
186 ε , rather than to any viscous attenuation.

187 **3. Systematic numerical studies of geophysical complexities**

188 *3.1. Influence of the length of the ellipsoid along the rotation axis*

189 Having validated our numerical code, we can investigate the influence of
 190 the aspect ratio c/b on the instability for a given ellipticity in the equatorial
 191 plane and a given rotation rate around the axis (Oz). This is directly re-
 192 lated to geo- and astro-physical flows as oblateness of planets, like the Earth
 193 for instance, is most of the time much stronger than its tidal deformation,
 194 meaning that the rotation axis is also the smallest one. The situation is even
 195 more pronounced in certain stars, as for instance Regulus A whose diame-
 196 ter is about 32% greater at the equator than the distance between its poles
 197 (McAlister et al., 2005).

198 Early theoretical work on this aspect was done by Kerswell (1994), who
 199 considered the inertial wave basis of an oblate spheroid ($a = b$) and calculated
 200 the first 60 subharmonic exact resonances and their growth rate for small
 201 ellipticities depending on the value of c (see also Kerswell and Malkus, 1998,
 202 for a special application to the case of Io). An explicit theoretical answer
 203 for the growth rate has also been found by Gledzer and Ponomarev (1992),
 204 starting from the base flow

$$\mathbf{u}_b = -\frac{a}{b} y \mathbf{e}_x + \frac{b}{a} x \mathbf{e}_y, \quad (5)$$

205 and looking for inviscid perturbations that are linear in space variables, cor-
 206 responding to the classical spin-over mode. Here, \mathbf{e}_x and \mathbf{e}_y are respectively
 207 the unit vectors of (Ox) and (Oy). In an open domain, the base flow (5)
 208 corresponds to elliptical streamlines with an ellipticity $\varepsilon = \frac{b^2 - a^2}{b^2 + a^2}$ as in our
 209 numerical model, but with a variable tangential velocity. As shown in figure

210 5, this base flow is a very good approximation of our configuration where we
 211 impose a constant tangential velocity on the elliptical boundary, outside a
 212 small boundary layer close to the external wall where recirculation cells take
 213 place. For such a flow, the inviscid growth rate determined by Gledzer and
 214 Ponomarev (1992) is:

$$\sigma = \sqrt{\frac{(b^2 - c^2)(c^2 - a^2)}{(b^2 + c^2)(a^2 + c^2)}} \quad (6)$$

215 Note that this theoretical growth rate is valid for $a \leq c \leq b$ only and is zero
 216 for $c = b$ or $c = a$. Then the maximal theoretical growth rate $\sigma_{\max} = \frac{b-a}{a+b}$ is
 217 obtained for $c = \sqrt{ab}$. One can notice that expression (3) leading to $\sigma = \frac{\varepsilon}{2}$
 218 in the inviscid case is recovered with $a = R_{eq} + s$ and $b = R_{eq} - s$ in the limit
 219 $\varepsilon \rightarrow 0$. Note also that the experimental choice $c = \frac{a+b}{2}$, equivalent to $c = \sqrt{ab}$
 220 for small ellipticities, results in the growth rate remaining very close to the
 221 maximum; for instance, even for an ellipticity of 0.7, the difference between
 222 the growth rate calculated for $c = \frac{a+b}{2}$ and the maximum value is only 2%.
 223 The numerical results are presented in figure 6. In order to compare them
 224 with the inviscid analytical prediction (6), a viscous damping term $-K\sqrt{E}$ is
 225 added to the expression of the inviscid growth rate, similarly to the classical
 226 expression (3). Excellent agreement is then found for $a \leq c \leq b$, again
 227 validating our approach. However, a slightly different constant $K = 2.5$
 228 (instead of 2.62 in (6), valid in the limit of small ε) allows a better fit of
 229 our data. For strong deformations, this constant clearly depends on the
 230 considered ellipticity; for instance, a similar study performed at $\varepsilon = 0.42$
 231 implies $K = 2.78$. Nevertheless, one can notice that K always remains
 232 about the same order of magnitude. One can also notice that because of the

233 scattering in the numerical results presented in figure 4 (a), such a constant
 234 $K = 2.5$ works equally well. Hence in the following, we systematically use
 235 $K = 2.5$.

236 In addition to the verification of the theoretical law of Gledzer and Pono-
 237 marev (1992), we are now in the position of exploring the range outside
 238 $a \leq c \leq b$, where other modes may grow that are not necessarily linear in
 239 space variables. As shown in figure 6, different modes of the elliptical insta-
 240 bility, characterized by their main frequency of oscillation, appear depending
 241 on the ratio c/b . In this view, the variation of the oblateness is similar to the
 242 variation of the aspect ratio in the case of an elliptically deformed cylinder
 243 (Eloy et al., 2003). Since the elliptical instability comes from the parametric
 244 resonance of two inertial waves of azimuthal wave number m and $m + 2$ with
 245 the underlying strain field, the corresponding mode is written $(m, m + 2)$
 246 and is related to a pulsation of frequency $\omega_{mode} = m + 1$. For instance, the
 247 spin-over mode corresponds to the stationary mode $(-1, 1)$ with half a wave-
 248 length along the axis of rotation. According to figure 6 (b), the mode $(1,3)$
 249 can be observed when $c < b$ and the mode $(0,2)$ when $c > a$. For even larger
 250 aspect ratio, the mode $(-1,1)$ with a larger wavenumber than the spin-over
 251 takes place. Note however that because of the geometrical confinement, no
 252 stationary mode can be excited for $c < b$.

253 *3.2. Influence of a background rotation*

254 In geo- and astrophysics, the tidal deformation of a given body (planet,
 255 moon or star) is also in rotation because of the orbital motion of the com-
 256 panion body. The influence of this background rotation on the develop-
 257 ment of the elliptical instability has been studied theoretically, using short-

258 wavelength analysis (Craik, 1989; Leblanc and Cambon, 1997; Le Dizès, 2000)
 259 or normal mode analysis (Gledzer and Ponomarev, 1992; Kerswell, 1994),
 260 and also numerically for specific vortices such as Stuart vortices (Leblanc
 261 and Cambon, 1998; Potylitsin and Peltier, 1999) or Taylor-Green vortices
 262 (Sipp et al., 1999). It has been studied experimentally in deformed cylinders
 263 (Vladimirov et al., 1983; Le Bars et al., 2007) and ellipsoids (Boubnov, 1978;
 264 Le Bars et al., 2010). All these works show that the background rotation has
 265 a stabilizing effect on cyclones and a destabilizing effect on anticyclones, ex-
 266 cept when the background rotation almost compensates for the flow rotation,
 267 in which case the elliptical instability disappears.

268 The theoretical expression of the growth rate for perturbations that are
 269 linear in space variables (i.e. corresponding to the classical spin-over mode)
 270 can be readily obtained by following the same method as Gledzer and Pono-
 271 marev (1992), but taking into account an additional Coriolis force coming
 272 from the background rotation at a given angular velocity $\Omega_c = \Omega_c^* \Omega$:

$$\sigma = \sqrt{\frac{(b^2 - c^2 + 2 \Omega_c^* a b)(c^2 - a^2 - 2 \Omega_c^* a b)}{(b^2 + c^2)(a^2 + c^2)}}. \quad (7)$$

273 Actually, this is a particular case of the more general stability analysis de-
 274 tailed in Cébron et al. (2010b) for a precessing triaxial ellipsoid. The ex-
 275 istence range of this mode is now between $c = b\sqrt{1 + 2\Omega_c^* a/b}$ and $c =$
 276 $a\sqrt{1 + 2 \Omega_c^* b/a}$ and the maximal theoretical growth rate is now exactly ob-
 277 tained for $\frac{c^2}{a b} = \Omega_c^* + \sqrt{1 + \Omega_c^* (a/b + b/a + \Omega_c^*)}$. In our numerical model,
 278 the addition of such a Coriolis force is straightforward and numerical results
 279 are presented in figure 7 (a). Again, they compare well with the theoretical
 280 prediction, providing that the viscous damping term, $-2.5\sqrt{E}$, found in sec-

281 tion 3.1 is added to the inviscid expression (7). Other modes are selected by
 282 the Coriolis force outside of the spin-over mode resonance band, as already
 283 observed experimentally by Le Bars et al. (2010).

284 Finally, we can investigate how the oblateness and the background rota-
 285 tion interact with each others. Considering for instance an oblate ellipsoid
 286 with a ratio c/b such as the mode (1, 3) is selected in absence of background
 287 rotation, the spin-over mode is recovered when decreasing Ω_c , as shown in
 288 figure 7 (b). More generally, we find that the $(-1, 1)$ mode is the most un-
 289 stable one in the anticyclonic domain up to a value $\Omega_c/\Omega_{tot} \lesssim -1$ where the
 290 flow restabilises, in agreement with the conclusions of Le Bars et al. (2010).

291 3.3. Influence of the obliquity of the ellipsoid

292 In planetary cores, tidal deformations are aligned with the orbital plane
 293 rather than with the equatorial plane, which means that they are not or-
 294 thogonal to the rotation axis. Previous works do not take into account this
 295 phenomenon, even though the obliquity can be significant, e.g. $23^\circ 26'$ for
 296 the Earth. In this section, we thus investigate the effect of obliquity for the
 297 first time and consider that, as a first approximation, the shape of the body
 298 remains a triaxial ellipsoid.

299 In the numerical model, the rotation axis is tilted and oriented along the
 300 unit vector $\mathbf{k}_c = (\cos(\phi) \sin(\theta), \sin(\phi) \sin(\theta), \cos(\theta))$, where ϕ is its azimuth
 301 angle and θ its colatitude angle in spherical coordinates (fig. 1). In assuming
 302 for example that the rotation axis is tilted in the (Oxz) plane (i.e. $\phi = 0$), we
 303 can study how the development of the elliptical instability changes depending
 304 on the obliquity θ . For $\theta = 0$, one recovers the usual configuration with $\varepsilon =$
 305 $\frac{b^2 - a^2}{b^2 + a^2}$ and an aspect ratio c/b . For $\theta = \pi/2$, one recovers results from section

306 3.1 in exchanging a and c , i.e. $\varepsilon = \frac{|b^2-c^2|}{b^2+c^2}$ and the aspect ratio is now a/b .
 307 In between, streamlines in planes perpendicular to the rotation axis are also
 308 elliptical, but their centers are not located along the rotation axis anymore,
 309 except in the equatorial plane $z = 0$. Besides the effective ellipticity measured
 310 in each plane now depends on z , the maximum being reached in the equatorial
 311 plane $z = 0$. Seen from this equatorial plane, the apparent length of the
 312 ellipsoid along the rotation axis is $\tilde{c} = \left(\frac{\sin^2 \theta}{a^2} + \frac{\cos^2 \theta}{c^2}\right)^{-\frac{1}{2}}$, whereas the great
 313 and small axes of the elliptical streamlines are respectively $\tilde{b} = b$ and $\tilde{a} =$
 314 $\left(\frac{\cos^2 \theta}{a^2} + \frac{\sin^2 \theta}{c^2}\right)^{-\frac{1}{2}}$. One can then estimate the growth rate of the instability
 315 using formulas (3) or (6) with these apparent lengths. Numerical results for
 316 the spin-over mode compared with these approximations are presented in
 317 figure 8. Results agree well for obliquity up to $\theta \sim 20^\circ$. Then, the numerical
 318 growth rate significantly differs, probably because the geometry is very far
 319 from an apparent ellipsoid in rotation around one of its principal axes. It
 320 remains however between the two expressions proposed. Note that for the
 321 Ekman number studied here, we do not see the tidal instability reappearing
 322 around $\theta \sim 90^\circ$, which will however be the case at smaller Ekman number:
 323 as seen in section 3.1, in this case other modes could appear because of the
 324 modified oblateness.

325 4. Scaling laws for global quantities of geophysical interest

326 4.1. Scaling law for the amplitude of the flow driven by the instability

327 The amplitude of the flow driven by the instability at saturation remains
 328 up to now an open question, mainly because it is determined by strong non-
 329 linear interactions. It is however an important quantity for geo- and astro-

330 physical applications, since it allows us to evaluate the influence of elliptical
 331 aspects compared to the other relevant ingredients of planetary dynamics,
 332 such as convection. In order to study the amplitude of the flow driven by the
 333 instability at saturation, we define the amplitude A^* by the maximum value
 334 over the volume V :

$$A^* = \max_V \|\mathbf{u} - \mathbf{u}_b\| \quad (8)$$

335 where \mathbf{u} is the dimensionless velocity field and \mathbf{u}_b is the theoretical base
 336 flow defined in section 3.1. The evolution of A^* as a function of the Ekman
 337 number is shown in figure 9 (a) for various ellipticities: it can be seen that
 338 A^* is not zero below the threshold of the elliptical instability because of
 339 the differences around the outer bound between the theoretical base flow
 340 and the flow numerically obtained (see figure 5). Actually, the difference
 341 is maximal on the boundary, along the smallest equatorial axis where the
 342 theoretical velocity is maximal. There, the corresponding amplitude $\lambda_{(\varepsilon)}$ can
 343 be calculated theoretically :

$$\lambda_{(\varepsilon)} = \frac{b}{\frac{a+b}{2}} - 1 = \frac{2}{1 + \sqrt{\frac{1-\varepsilon}{1+\varepsilon}}} - 1 \quad (9)$$

344 which only depends on ε . One then defines the amplitude of the flow driven
 345 by the instability by $A = A^* - \lambda_{(\varepsilon)}$, which is equal to 0 below the threshold
 346 (fig. 9 (b)).

347 Far from threshold, a secondary instability appears, which induces a sec-
 348 ondary dynamics superimposed on the primary state : e.g. typically, for
 349 $\varepsilon = 0.317$, $E = 1/1500$, $c = \frac{a+b}{2}$, the spinover mode is no more stationary,
 350 and the flow is slightly oscillating around the spinover mean flow, at a pul-
 351 sation $\omega_{sec} \approx 1.4$. Note that this is in agreement with Kerswell (2002) which

352 predicts that the primary elliptical instability should saturate and be stable
 353 only in a small strain window $\varepsilon - \varepsilon_c = O(E)$. Thus, the amplitude A has to
 354 be averaged in time to smooth out the small scale fluctuations. Since those
 355 small-scale fluctuations take place on a typical time scale comparable to one
 356 revolution $2\pi/\Omega$, whereas the characteristic time for the tidal instability is
 357 the inverse of the growth rate, i.e. $(\Omega \varepsilon/2)^{-1}$, the averaging is performed
 358 about a typical time $\Omega^{-1}\sqrt{4\pi/\varepsilon}$ corresponding to the geometrical mean of
 359 these two extreme values.

360 With this definition, figure 9 (b) shows that all results collapse on the
 361 same generic law above the threshold providing that we use the variable
 362 $E_c/E - 1$. Far from threshold, the amplitude seems to saturate around 1,
 363 which means that the velocities generated by the tidal instability are com-
 364 parable to the imposed boundary rotation.

365 One can notice that near the threshold, a square root $A \approx 0.6 \sqrt{E_c/E - 1}$
 366 fits the results, which is in agreement with a pitchfork bifurcation. Actually,
 367 this scaling law can be obtained analytically, starting from the simple model
 368 used in Lacaze et al. (2004) to describe the viscous non-linear evolution of the
 369 spinover mode. This model, first introduced by Hough (1895) and Poincaré
 370 (1910) for an inviscid solid-body rotation in a spheroid, reduces to:

$$371 \quad \dot{\omega}_x = -\alpha (1 + \omega_z) \omega_y - \nu_{so} \omega_x \quad (10)$$

$$372 \quad \dot{\omega}_y = -\beta (1 + \omega_z) \omega_x - \nu_{so} \omega_y \quad (11)$$

$$\dot{\omega}_z = \varepsilon \omega_x \omega_y - \nu_{ec} \omega_z + \nu_{nl} (\omega_x^2 + \omega_y^2) \quad (12)$$

373 where $\boldsymbol{\omega}$ is the rotation vector of the spinover mode, $\alpha = \frac{\varepsilon}{2-\varepsilon}$ and $\beta =$
 374 $\frac{\varepsilon}{2+\varepsilon}$. The damping terms are given by theory (no adjustable parameter):

375 $\nu_{so} = 2.62 \sqrt{E}$ is the linear viscous damping rate of the spinover mode (first
 376 calculated by Greenspan (1968)), $\nu_{ec} = 2.85 \sqrt{E}$ is the linear viscous damping
 377 of axial rotation and $\nu_{nl} = 1.42 \sqrt{E}$ is the viscous boundary layer effect on
 378 the non-linear interaction of the spinover mode with itself (see Greenspan
 379 (1968)). Even if this model does not take into account all the viscous terms
 380 of $O(\sqrt{E})$ or the non-linear corrections induced by the internal shear layers,
 381 it satisfyingly agrees with experiments, regarding the growth rate as well as
 382 the non-linear saturation (Lacaze et al., 2004). Thus, this model can be used
 383 with confidence to describe the viscous non-linear evolution of the spinover
 384 mode.

385 After little algebra, we obtain a non-trivial stationary state for $\varepsilon > 2\nu_{so}$,
 386 given by:

$$\omega_x = \pm \sqrt{\frac{\nu_{ec} [\sqrt{\alpha\beta} - \nu_{so}]}{\beta \varepsilon - \nu_{nl} [\sqrt{\alpha\beta} + \beta^2/\sqrt{\alpha\beta}]}} \approx \pm \sqrt{\frac{\nu_{ec} [\varepsilon - 2 \nu_{so}]}{\varepsilon^2 - 2 \nu_{nl} \varepsilon}} \quad (13)$$

387

$$\omega_y = \mp \sqrt{\frac{\nu_{ec} [\sqrt{\alpha\beta} - \nu_{so}]}{\alpha \varepsilon - \nu_{nl} [\sqrt{\alpha\beta} + \alpha^2/\sqrt{\alpha\beta}]}} \approx \mp \sqrt{\frac{\nu_{ec} [\varepsilon - 2 \nu_{so}]}{\varepsilon^2 - 2 \nu_{nl} \varepsilon}} \approx \mp \omega_x \quad (14)$$

388

$$\omega_z = \frac{\nu_{so}}{\varepsilon} \sqrt{4 - \varepsilon^2} - 1 \approx \frac{2 \nu_{so}}{\varepsilon} - 1 \quad (15)$$

389 where approximations are done assuming $\varepsilon \ll 1$. Now, the amplitude A
 390 corresponds to the norm of the flow $\boldsymbol{\omega} \times \mathbf{r}$ driven by the spinover mode.

391 Then, near the threshold ($\varepsilon \approx 2 \cdot 2.62\sqrt{E_c}$ and $E_c/E - 1 \ll 1$), we obtain:

$$A \approx \sqrt{\frac{\nu_{ec}}{2(\nu_{so} - \nu_{nl})} \left(\frac{E_c}{E} - 1 \right)} \approx 1.1 \sqrt{\frac{E_c}{E} - 1} \quad (16)$$

392 which is in good agreement with the numerical fit.

393 *4.2. Scaling law for the viscous dissipation by the instability*

394 As explained for instance in Rieutord (2003) or in Le Bars et al. (2010),
 395 the energy dissipated by tides is a primordial quantity which directly influ-
 396 ences the orbital evolution and rotational history of a binary system during
 397 its synchronization. It is however poorly known (e.g. Williams, 2000; Touma
 398 and Wisdom, 1994). In most traditional models, fluid dissipation in the plan-
 399 etary core is supposed to be negligible. However this may not be the case
 400 when the elliptical instability is excited at a rather large amplitude, inducing
 401 important shears between the bulk of the fluid and the boundary. Our pur-
 402 pose here is to systematically quantify the variation of this dissipation with
 403 the ellipticity and the Ekman number.

404 The dissipated power balance of the incompressible flow in the ellipsoid
 405 is given by:

$$\iiint_V \frac{\partial}{\partial t} \left(\rho \frac{\tilde{u}^2}{2} \right) d\tau = \iint_S (\bar{\bar{\boldsymbol{\sigma}}}_v \cdot \mathbf{n}) \cdot \tilde{\mathbf{u}} ds - \iiint_V \bar{\bar{\boldsymbol{\sigma}}}_v : \nabla \tilde{\mathbf{u}} d\tau \quad (17)$$

406 where $\bar{\bar{\boldsymbol{\sigma}}}_v = \eta (\nabla \tilde{\mathbf{u}} + {}^t \nabla \tilde{\mathbf{u}})$ is the viscous stress tensor of the newtonian
 407 fluid, S the surface of the ellipsoid, $\tilde{\mathbf{u}} = \Omega R_{eq} \mathbf{u}$ is the dimensionalized
 408 velocity field, ρ the volumic mass and η the dynamic viscosity of the fluid.
 409 In this section, we focus on the stationary spinover mode and then the two
 410 terms on the right side of equation (17) balance each others: the first one
 411 allows to maintain the rotation of the fluid by the no-slip conditions on the
 412 boundary while the second one is the volume dissipation P of the fluid. In
 413 the following, we use as a power scale the dissipated power during the spin-
 414 down stage of the equivalent sphere of radius R_{eq} and moment of inertia I_Δ
 415 ($I_\Delta = 2/5 MR^2$ for an homogeneous sphere of mass M and radius R), i.e. the

416 kinetic energy of rotation $E_c = \frac{1}{2} I_\Delta \Omega^2$ divided by the Ekman time t_E . Note
 417 that most of the dissipated power comes naturally from the boundary layers:
 418 its determination is thus a challenging task from a numerical point of view,
 419 and extra care must be taken regarding the convergence of the simulations,
 420 as shown for instance in figure 2 (b).

421 Below the threshold, the dissipated power is not zero because of the re-
 422 circulation patterns of our base flow (see figure 5). This dissipation is due
 423 to the flow driven by the ellipticity, which scales as $\varepsilon \Omega R$ for small elliptici-
 424 ties. Then, the dimensionalized dissipated power below the threshold simply
 425 scales as

$$\iiint_V \bar{\boldsymbol{\sigma}}_v : \nabla \tilde{\mathbf{u}} \, d\tau \sim \eta \varepsilon^2 \Omega^2 R^3 \quad (18)$$

426 which is confirmed by the dissipated power measured in our numerical sim-
 427 ulations below the threshold.

428 Far from threshold, the model proposed by Le Bars et al. (2010) considers
 429 that the spin-over mode simply corresponds to a supplementary solid body
 430 rotation $\boldsymbol{\Omega}_{\text{SO}}$ outside the outer viscous boundary layer of thickness $h =$
 431 $\xi \sqrt{\nu/\Omega_{\text{SO}}}$, ξ being a constant of order 1. Then, the dissipation is only
 432 located in this boundary layer, where the fluid rotation has to match the
 433 imposed velocity conditions at the outer boundary. With this simple model,
 434 the torque of the container on the fluid is $\mathbf{C}^{\text{m/c}} = -2 M \nu \frac{R}{h} \boldsymbol{\Omega}_{\text{SO}}$, and the
 435 power dissipated by the system is $P = -2 M \nu \frac{R}{h} \Omega_{\text{SO}}^2$, which can also be
 436 written $P = -\frac{2}{\xi} M R \sqrt{\nu} \Omega^{5/2} A^{5/2}$, where A is the dimensionless spin-over
 437 mode amplitude studied in the previous section. The dimensionless power

438 given by this model can finally be stated as

$$P_{dissip} = \frac{|P|}{\frac{1}{2} I_{\Delta} \Omega^3 \sqrt{E}} = \frac{10}{\xi} A^{5/2}, \quad (19)$$

439 where, according to the previous section, A is about 1 in the small Ekman
440 number limit studied here.

441 The evolution of P_{dissip} measured in our numerical model is shown in fig-
442 ure 10. It confirms the behavior predicted by (19) with a saturation far from
443 threshold and $\xi \approx 1$. This behavior is especially interesting for planetary
444 applications, as will be studied in the following section.

445 5. Orders of magnitude for planetary applications

446 From a geophysical point of view, the results from the previous sections
447 can be used to derive the orders of magnitude involved in planetary cores.
448 Regarding the jovian moon Io, which is clearly unstable to the tidal instability
449 and where the strong tidal dissipation is a topical question (Lainey et al.,
450 2009), our numerical study confirms the first trends given by Le Bars et al.
451 (2010), with however a numerically determined scaling factor of the order
452 $1/\xi \approx 1$ in the power dissipation estimates. Moreover, the most important
453 result comes from the oblateness effects. Indeed, according to the data given
454 in Kerswell and Malkus (1998), $c/b \sim 0.995$ and $a/b > 0.999$, which means
455 that the excited mode of the tidal instability in Io cannot be the spin-over
456 mode, but has to be oscillatory. Note that this result is not modified when
457 the background rotation is taken into account.

458 A similar analysis can be done for the early Earth, with a Moon two
459 times closer than today. In this case, the length of the day was around

460 10 hours according to Touma and Wisdom (1994) and the lunar tides were
461 around eight times stronger, whereas the solar tides were about the same.
462 Then, the actual tidal amplitude of 50 cm allows to estimate the ellipticity
463 of the early Earth: $\varepsilon \sim 10^{-6}$. In considering a similar but totally molten
464 core, we estimate $E_c/E - 1 \sim 70$, which means that the early Earth's core
465 was clearly unstable to tidal instability, and that the tidal instability was
466 then at saturation. Moreover, with an orbital period for the Moon $(1/2)^{3/2}$
467 shorter than the actual moon (Kepler's Third Law), the dissipated power
468 given by the model was around $P \sim 10^{18} W$. This estimation seems huge
469 in comparison with the present dissipation by tidal friction ($\sim 3.75 \cdot 10^{12} W$
470 according to Munk (1998)) but actually, it simply suggests that the Earth-
471 Moon system was then in rapid evolution. Once again, the possible mode
472 of the tidal instability was not the spin-over mode neither any stationary
473 $(-1, 1)$ mode, considering that the oblateness of the rapidly rotating early
474 Earth was larger than the actual oblateness. In fact, we expect stationary
475 modes to be only marginally excited in geophysical systems, limited to very
476 peculiar configuration regarding the oblateness and the rotation of the tidal
477 bulge.

478 Note that computations similar to the ones presented here for an ellip-
479 soidal geometry have been performed for an ellipsoidal shell in order to study
480 the influence of a solid inner planetary core. Similar conclusions are then
481 found regarding the physics of the tidal instability. Only a slightly larger
482 dissipation term due to the presence of an inner viscous boundary layer has
483 to be taken into account.

484 **6. Conclusion**

485 This paper presents the first systematic numerical study of the tidal in-
486 stability in a rotating ellipsoid. The numerical approach is a powerful tool to
487 complete the knowledge derived from previous theoretical and experimental
488 studies. The effects of oblateness, background rotation and obliquity, which
489 lead to the selection of various instability modes, have been studied. We
490 have also defined scaling laws regarding the amplitude of the flow driven by
491 the instability and its viscous dissipation, which confirm the primordial role
492 played by tidal effects at a planetary scale.

493 Another fundamental geophysical issue regarding the elliptical instability
494 is whether or not it can drive a planetary dynamo. The results presented
495 herein show that the numerical approach is able to faithfully capture the
496 physics of the hydrodynamic elliptical instability. Thus, the present work
497 provides a solid basis to study the full MHD problem encountered in plane-
498 tary core flows undergoing tidal instability. These flows can only be studied
499 numerically due to their inherent complexity. Therefore, a next step will be
500 to introduce the effects of a magnetic field in our model.

501 **References**

- 502 Aldridge, K., Seyed-Mahmoud, B., Henderson, G., van Wijngaarden, W.,
503 1997. Elliptical instability of the Earth's fluid core. *Phys. Earth Planet.*
504 *Int.* 103, 365–74.
- 505 Bayly, B. J., 1986. Three-dimensional instability of elliptical flow. *Phys. Rev.*
506 *Lett.* 57, 2160 - 2163

- 507 Benton, E.R., Clark, A., 1974. Spin-Up. *Annu. Rev. Fluid. Mech.* 6, 257–280.
- 508 Boubnov, B. M., 1978. Effect of Coriolis force field on the motion of a fluid
509 inside an ellipsoidal cavity. *Izv. Atmos. Ocean. Phys.*, 14, 501-504.
- 510 Cadot, O., Douady, S., Couder, Y., 1995. Characterization of the low pressure
511 filaments in three-dimensional turbulent shear flow. *Phys. Fluids* 7, 630–
512 646.
- 513 Cébron, D., Maubert, P., Le Bars, M., 2010. Tidal instability in a rotating
514 and differentially heated ellipsoidal shell. *Geophys. J. Int.* In revision.
- 515 Cébron, D., Le Bars, M., Meunier, P., 2010. Tilt-over mode in a precessing
516 triaxial ellipsoid. *Phys. Fluids.* In revision.
- 517 Craik, A. D. D., 1989. The stability of unbounded two- and three-dimensional
518 flows subject to body forces: some exact solutions. *J. Fluid Mech.* 198, 275–
519 292.
- 520 Chan, K. H, Zhang, K., Liao, X., 2010. An EBE finite element method
521 for simulating nonlinear flows in rotating spheroidal cavities. *International*
522 *Journal for Numerical Methods in Fluids* Volume 63 Issue 3, Pages 395 -
523 414
- 524 Eloy, E., Le Gal, P., Le Dizès, S., 2000. Experimental study of the multipolar
525 vortex instability. *Phys. Rev. Lett.* 85, 145–166.
- 526 Eloy, E., Le Gal, P., Le Dizès, S., 2003. Elliptic and triangular instabilities
527 in rotating cylinders. *J. Fluid Mech.* 476, 357–388.

- 528 Greenspan, H. P., 1968. *The Theory of Rotating Fluids*, Cambridge Univer-
529 sity Press, Cambridge.
- 530 Herreman, W., Le Bars, M., Le Gal, P., 2009. On the effects of an imposed
531 magnetic field on the elliptical instability in rotating spheroids. *Phys. Flu-*
532 *ids* 21, 046602.
- 533 Gledzer, E. B., Ponomarev, V. M., 1977. Finite dimensional approximation
534 of the motions of incompressible fluid in an ellipsoidal cavity. *Izv. Atmos.*
535 *Ocean. Phys.* 13, 565–569.
- 536 Gledzer, E. B., Ponomarev, V. M., 1992. Instability of bounded flows with
537 elliptical streamlines. *J. Fluid Mech.* 240, 1–30.
- 538 Gledzer, E. B., Dolzhansky, F. V., Obukhov, A. M., Ponomarev, V. M., 1975.
539 An experimental and theoretical study of the stability of motion of a liquid
540 in an elliptical cylinder. *Izv. Atmos. Ocean. Phys.* 11, 617–622.
- 541 Haj-Hariri, H., Homsy, G. M., 1997. Three-dimensional instability of vis-
542 coelastic elliptic vortices. *J. Fluid Mech.* 353, 357–381.
- 543 Hindmarsh, A. C., Brown, P. N., Grant, K. E., Lee, S. L., Serban, R., Shu-
544 maker, D. E., Woodward, C. S., 2005. SUNDIALS: Suite of Nonlinear and
545 Differential/Algebraic Equation Solvers. *ACM T. Math. Software*, vol. 31,
546 p. 363.
- 547 Hollerbach, R., Kerswell, R. R., 1995. Oscillatory internal shear layers in
548 rotating and precessing flows. *J. Fluid Mech.* 298, 327–339.

- 549 Hough, S. S., 1895. The oscillations of a rotating ellipsoidal shell containing
550 fluid. *Phil. Trans. A* 186, 469–506.
- 551 Kerswell, R. R., 1994. Tidal excitation of hydromagnetic waves and their
552 damping in the Earth. *J. Fluid Mech.* 274, 219–241.
- 553 Kerswell, R. R., 2002. Elliptical instability. *Annu. Rev. Fluid. Mech.* 34, 83–
554 113.
- 555 Kerswell, R. R., Malkus, W. V. R., 1998. Tidal instability as the source for
556 Io’s magnetic signature. *Geophys. Res. Lett.* 25, 603–6.
- 557 Kelvin, L., 1880. Vibrations of a columnar vortex. *Phil. Mag.* 10, 155–168.
- 558 Kudlick, M., 1966. On the transient motions in a contained rotating fluid.
559 PhD thesis, MIT.
- 560 Lacaze, L., Herreman, W., Le Bars, M., Le Dizès, S., Le Gal, P., 2006. Mag-
561 netic field induced by elliptical instability in a rotating spheroid. *Geophys.*
562 *Astrophys. Fluid Dyn.* 100, 299–317.
- 563 Lacaze, L., Le Gal, P., Le Dizès, S., 2004. Elliptical instability in a rotating
564 spheroid. *J. Fluid Mech.* 505, 1–22.
- 565 Lacaze, L., Le Gal, P., Le Dizès, S., 2005. Elliptical instability of the flow in
566 a rotating shell. *Phys. Earth. Planet. Int.*, 151, pp. 194-205
- 567 Lacaze, L., Ryan, K., Le Dizès, S., 2007. Elliptic instability in a strained
568 Batchelor vortex. *J. Fluid Mech.* 577, 341

- 569 Lainey, V., Arlot, J. E., Karatekin, O., Van Hoolst, T., 2009. Strong tidal
570 dissipation in Io and Jupiter from astrometric observations. *Nature* 459,
571 957-959.
- 572 Le Bars, M., Lacaze, M., Le Dizès, S., Le Gal, P., Rieutord, M., 2010. Tidal
573 instability in stellar and planetary binary system. *Phys. Earth. Planet.*
574 *Int.*, 178, Issues 1-2, January 2010, Pages 48-55.
- 575 Le Bars, M., Le Dizès, S., Le Gal, P., 2007. Coriolis effects on the elliptical
576 instability in cylindrical and spherical rotating containers. *J. Fluid Mech.*
577 585, 323-342.
- 578 Leblanc, S., Cambon, C., 1997. On the three-dimensional instabilities of
579 plane flows subjected to Coriolis force. *Phys. Fluids* 9, 1307.
- 580 Leblanc, S., Cambon, C., 1998. Effects of the Coriolis force on the stability
581 of Stuart vortices. *J. Fluid Mech.* 356, 353-379.
- 582 Le Dizès, S., 2000. Three-dimensional instability of a multipolar vortex in a
583 rotating flow. *Phys. Fluids* 12, 2762-74.
- 584 Le Dizès, S., Laporte, F., 2002. Theoretical predictions for the elliptic insta-
585 bility in a two-vortex flow. *J. Fluid Mech.* 471, 169-201.
- 586 Leweke, T., Williamson, C. H. K., 1998. Three-dimensional instabilities in
587 wake transition. *Eur. J. Mech. B/Fluids* 17, 571-586.
- 588 Leweke, T., Williamson, C. H. K., 1998. Cooperative elliptic instability of a
589 vortex pair. *J. Fluid Mech.* 360, 85-119.

- 590 Lundgren, T. S., Mansour, N. N., 1995. Transition to turbulence in an elliptic
591 vortex. *J. Fluid Mech.* 307, 43–62.
- 592 Malkus, W. V. R., 1968. Precession of the Earth as the cause of geomag-
593 netism. *Science* 160, 259–264.
- 594 Malkus, W. V. R., 1989. An experimental study of global instabilities due to
595 tidal (elliptical) distortion of a rotating elastic cylinder. *Geophys. Astro-
596 phys. Fluid Dyn.* 48, 123–134.
- 597 Mason, D. M., Kerswell, R. R., 1999. Nonlinear evolution of the elliptical
598 instability: an example of inertial wave breakdown. *J. Fluid Mech.* 396,
599 73–108.
- 600 Meunier, P., Ehrenstein, U., Leweke, T., Rossi, M., 2002. A merging criterion
601 for two-dimensional co-rotating vortices. *Phys. Fluids* 14, 2757–2766.
- 602 McAlister, H. A., Ten Brummelaar, T. A., Gies, D. R., Huang, W. , Bag-
603 nuolo, W. G., Shure, M. A., Sturmman, J., Sturmman, L., Turner, N. H.,
604 Taylor, S. F., Berger, D. H., Baines, E. K., Grundstrom, E., Ogden, C.,
605 Ridgway, S. T., van Belle, G., 2005. First results from the CHARA array.
606 I. An interferometric and spectroscopic study of the fast rotator α Leonis
607 (Regulus). *The Astrophysical journal*, vol. 628 (1), no1, pp. 439-452.
- 608 Moore, D. W., Saffman, P. G., 1975. The instability of a straight vortex
609 filament in a strain field. *Proc. R. Soc. Lond. A* 346, 413–425.
- 610 Munk, W., 1998. Abyssal recipes II: energetics of tidal and wind mixing. *Deep
611 Sea Res. Part I. Oceanographic Research*, vol. 45, no12, pp. 1977-2010.

- 612 Owen, J. M., Rogers, R. H., 1989. Flow and heat transfer in rotating disc
613 systems (Vol. 1, Rotor-stator systems). Research Studies Press, Taunton,
614 UK and John Wiley, NY.
- 615 Pierrehumbert, R. T., 1986. Universal short-wave instability of two-
616 dimensional eddies in an inviscid fluid. *Phys. Rev. Lett.* 57, 2157 - 2159.
- 617 Poincaré, R., 1910. Sur la précession des corps déformables. *Bull. Astr.* 27
618 (1910) 321.
- 619 Potylitsin, S., Peltier, W. R., 1999. Three-dimensional destabilization of
620 Stuart vortices: the influence of rotation and ellipticity. *J. Fluid Mech.*
621 387,205-226.
- 622 Rieutord, M., 2003. Evolution of rotation in binaries: physical processes.
623 *Stellar Rotation, Proc. IAU Symp.* 215, 394–403.
- 624 Roy, M., Schaeffer, N., Le Dizès, S., Thompson M. C., 2007. Stability of a
625 pair of co-rotating vortices with axial flow. *Phys. Fluids* 20, 094101.
- 626 Seyed-Mahmoud, B., Aldridge, K. D., Henderson, G., 2004. Elliptical insta-
627 bility in rotating spherical fluid shells: application to Earth's fluid core.
628 *Phys. Earth Planet. Int.* 142, 257–282.
- 629 Seyed-Mahmoud, B., Henderson, G., Aldridge, K. D., 2000. A numerical
630 model for elliptical instability of the Earth's fluid outer core. *Phys. Earth*
631 *Planet. Int.* 117, 51–61.
- 632 Shangli, O., Henderson, J. E., Motl, P. M., 2007. Further evidence for an

- 633 elliptical instability in rotating fluid bars and ellipsoidal stars. *Astrophys.*
634 *J.* 665,1074
- 635 Sipp, D., Jacquin, L., 1998. Elliptic instability in two-dimensional flattened
636 Taylor–Green vortices. *Phys. Fluids* 10, 839.
- 637 Sipp, D., Lauga, E., Jacquin, L., 1999. Vortices in rotating systems: Cen-
638 trifugal, elliptic and hyperbolic type instabilities. *Phys. Fluids*, vol. 11,
639 Issue 12, 3716.
- 640 Thess, A., Zikanov, O., 2007. Transition from two-dimensional to three-
641 dimensional magnetohydrodynamic turbulence. *J. Fluid Mech.*, 579, p.
642 383-412.
- 643 Touma, J., Wisdom, J., 1994. Evolution of the Earth-Moon system. *The*
644 *Astr. J.*, vol. 108, no. 5, p. 1943-1961.
- 645 Vladimirov, V. A., Tarasov, V. F., Rybak, L. Ia., 1983. The stability of the
646 elliptically deformed rotation of an ideal incompressible fluid in a Coriolis
647 force field. *Izv. Atmos. Ocean. Phys.*, 14, 501-504.
- 648 Waleffe, F. A., 1990. On the three-dimensional instability of strained vortices.
649 *Phys. Fluids* 2, 76–80.
- 650 Widnall, S. E., Bliss, D., Tsai, C.-Y, 1974. The instability of short waves on
651 a vortex ring. *J. Fluid Mech.* 66, 35–47.
- 652 Williams, G. E., 2000. Geological constraints on the Precambrian history of
653 Earth’s rotation and the Moon’s orbit. *Reviews of Geophysics*, Volume 38,
654 Issue 1, p. 37-60.

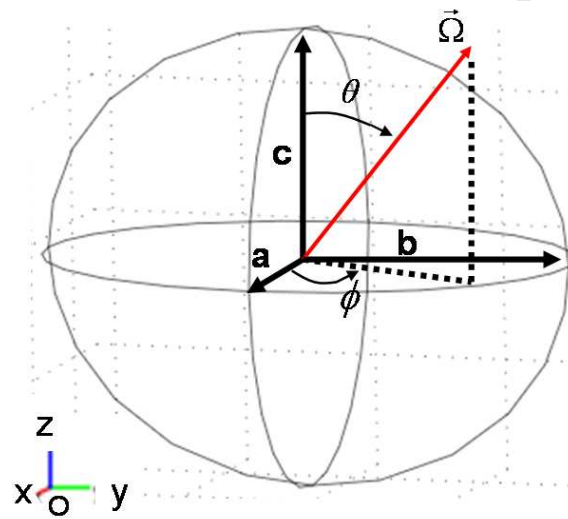


Figure 1: *Sketch of the problem under consideration : a rotating flow inside a triaxial ellipsoid of axes (a, b, c) related to a frame (Ox, Oy, Oz) with a constant tangential velocity all along the boundary in each plane perpendicular to the rotation vector Ω .*

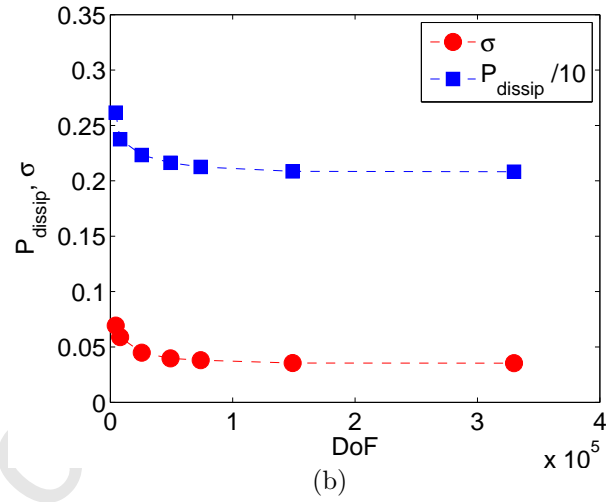
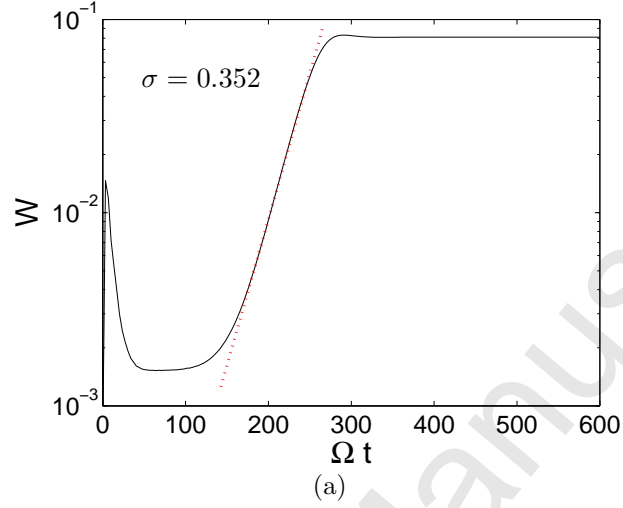
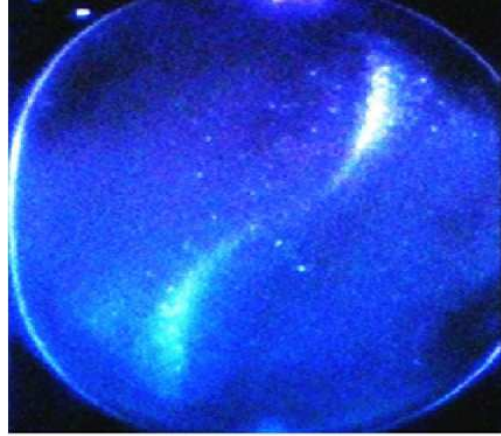
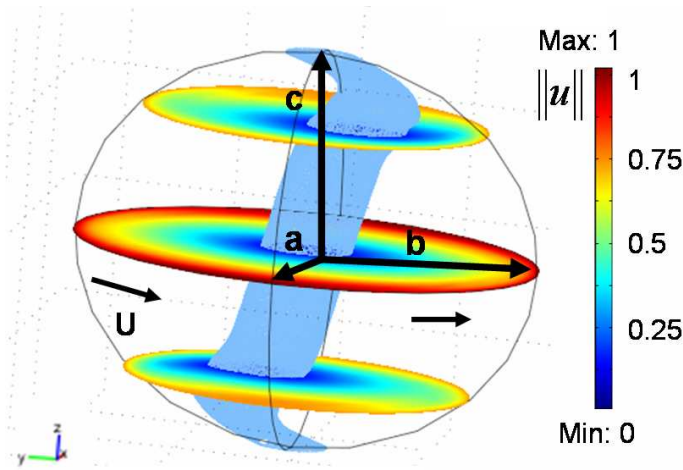


Figure 2: Simulations performed at $E = 1/500$ and $\varepsilon = 0.317$ for $c = \frac{a+b}{2}$. (a) Time evolution of the mean value of the vertical velocity, showing the spin-up phase ($\Omega t_E \approx 22$), the exponential growth of the tidal instability (see also in dotted line the exponential fit with a growth rate $\sigma = 0.352$) and its saturation. (b) Convergence with the number of degrees of freedom (DoF) of the growth rate σ and of the dissipated power P_{dissip} at saturation. Results presented in (a) are computed for 42459 DoF.



(a)



(b)

Figure 3: Validation of the numerical simulations. (a) Kallirosopic visualization of the spin-over mode in the meridional plane of maximum shear for $E = 1/4000$ and $\varepsilon = 0.16$. The typical S shape of the rotation axis is due to the combination of the main rotation imposed by the boundary and the spin-over mode. (b) Slices of the velocity field $\|\mathbf{u}\|$ and surface of iso-value $\|\mathbf{u}\| = 0.15$ at saturation of the tidal instability for $E = 1/344$, $\varepsilon = 0.317$, $c = \frac{a+b}{2}$, and 49900 DoF. The classical S-shape of the spin-over mode is recovered.

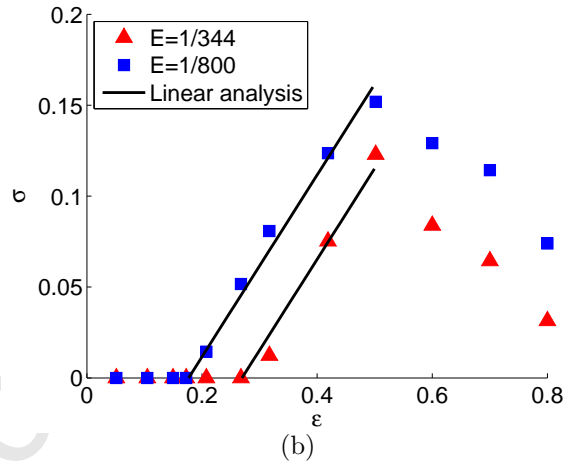
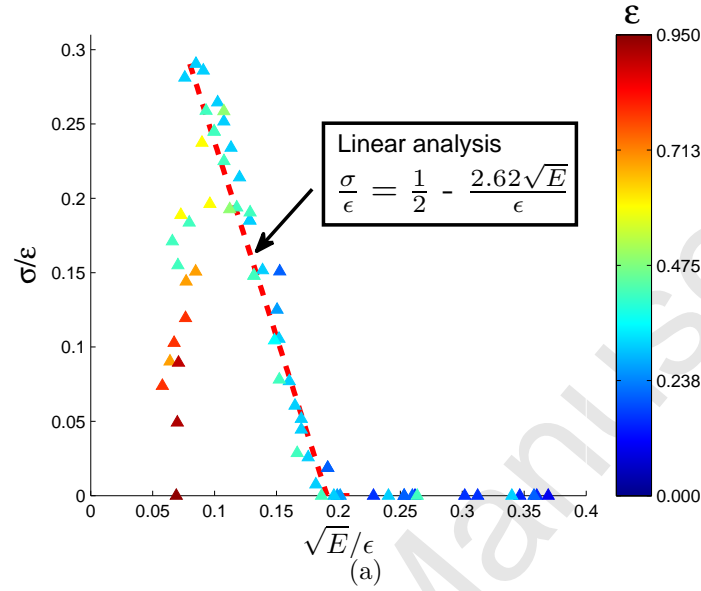


Figure 4: Validation of the numerical simulations. (a) Evolution of the growth rate for ($E \geq 1/2000$, $\varepsilon \leq 0.95$, $c = \frac{a+b}{2}$) and comparison with the linear theory indicated by a dashed line. The coefficient 2.62 comes from Lacaze et al. (2004) and is valid in the limit of small ellipticity. Good agreement is found for values of ε up to 0.5. (b) Evolution of the growth rate depending on the ellipticity for two values of the Ekman number $E = 1/344$ and $E = 1/800$ ($\varepsilon \leq 0.8$, $c = \frac{a+b}{2}$). As also seen in (a), the growth rate agrees with the linear analytical analysis close to the threshold and then decreases for large values of the ellipticity.

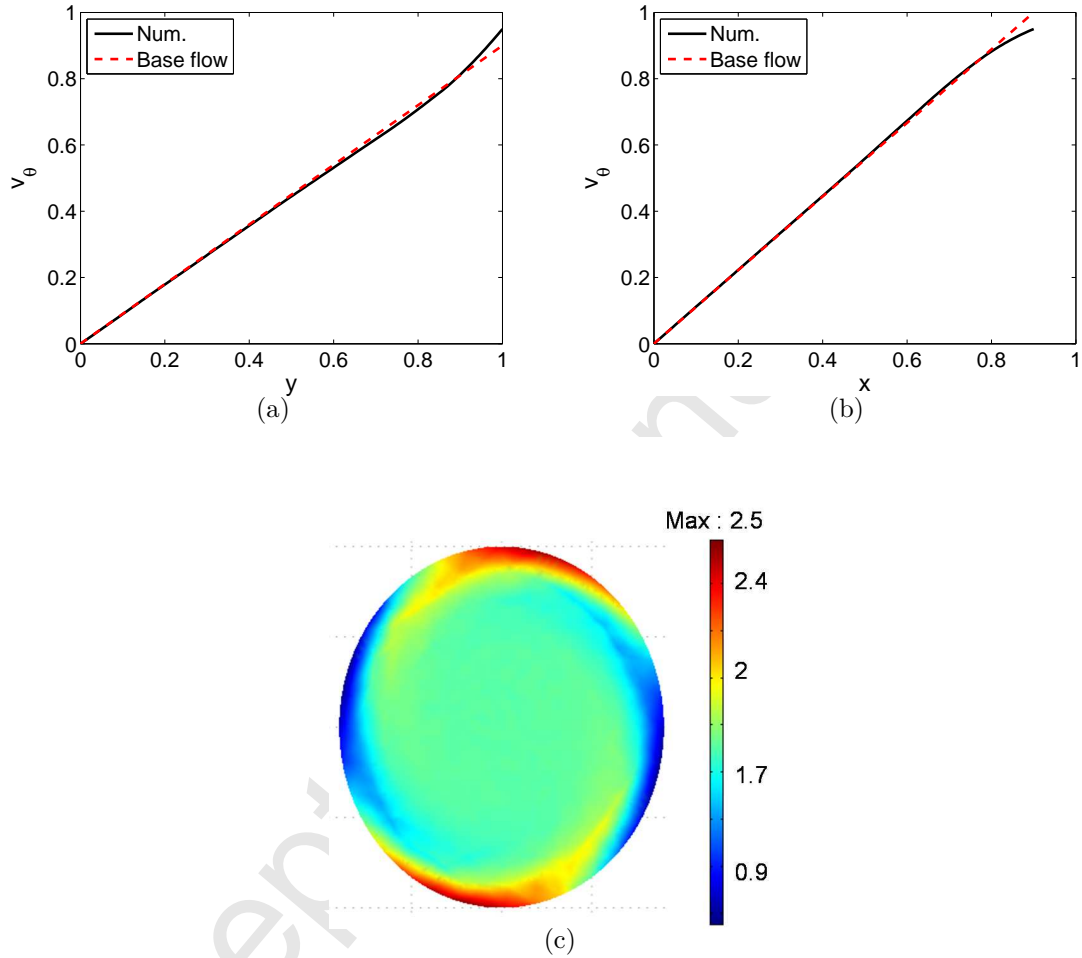


Figure 5: Azimuthal velocity v_θ for $E = 1/95$, $\varepsilon = 0.1$, $c = \frac{a+b}{2}$. (a) Slice along (Oy) at $x = 0$. (b) Slice along (Ox) at $y = 0$. (c) Slice in the equatorial plane of the vertical component of the vorticity. Dashed lines in (a) and (b) correspond to the theoretical base flow (5), which presents a variable tangential velocity along elliptical streamlines. Good agreement is found with the numerical results, except in the small outer viscous boundary layer, where recirculation cells take place to match the imposed constant velocity along the boundary. Note in particular that the maximum velocity is not reached at the boundary but within this viscous boundary layer.

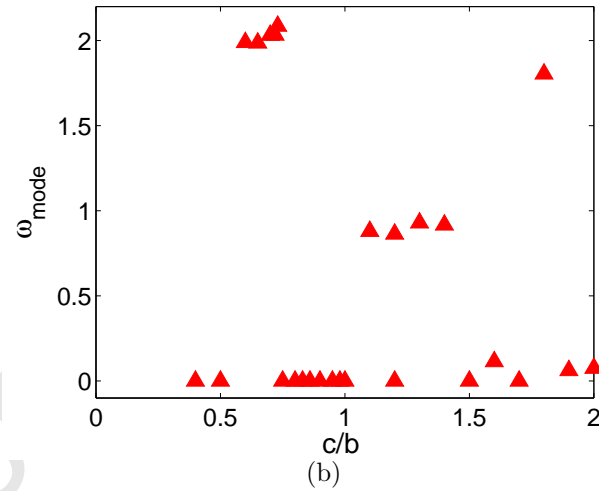
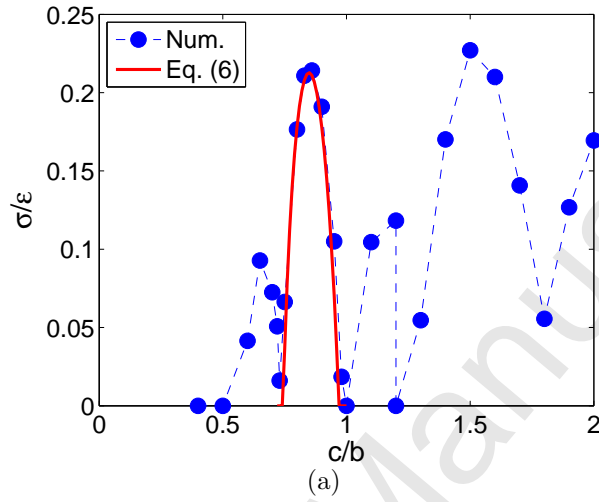


Figure 6: Influence of the length of the ellipsoid along the rotation axis on the mode selection of the tidal instability ($E = 1/688, \varepsilon = 0.317$). (a) Variation of the growth rate. (b) Variation of the main frequency of the selected mode determined by Fourier analysis of its saturation state.

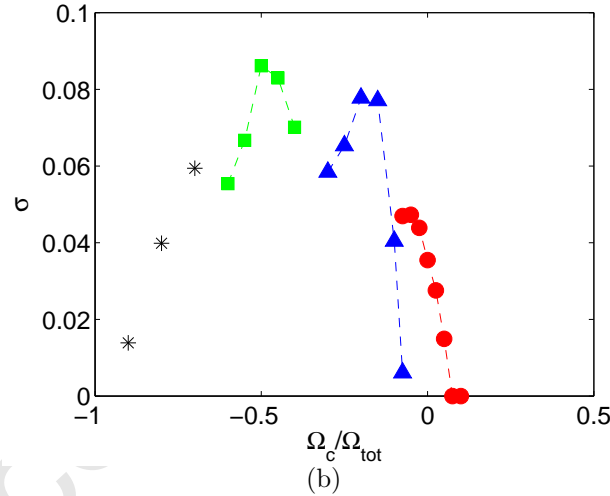
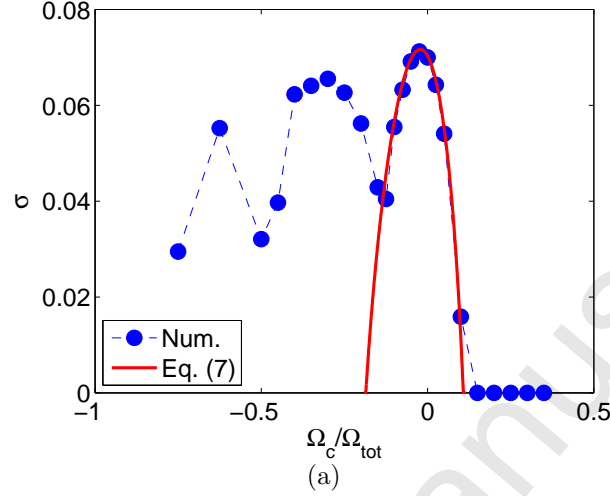


Figure 7: Evolution of the growth rate in the presence of a background rotation for a fixed ellipticity $\varepsilon = 0.317$ and a fixed value of the total Ekman number $E_{tot} = \frac{\nu}{\Omega_{tot} R_{eq}^2} = 10^{-3}$, where Ω_{tot} takes into account the background rotation and the fluid rotation, i.e. $\Omega_{tot} = \Omega_c + \Omega$. (a) $c = (a + b)/2$, i.e. $c/b = 0.86$: the spin-over mode is then excited in the absence of background rotation. Good agreement is found around this value with the analytical solution (7). Further decreasing Ω_c , other modes with smaller wavelength along the rotation axis appear. (b) $c/b = 0.65$: the (1,3) mode is then excited in the absence of background rotation. Other modes can be excited: \bullet represent the (1,3) mode, \blacktriangle the spin-over mode, \blacksquare represent the (-1,1) mode with one wavelength along the axis of rotation, and $*$ are other modes.

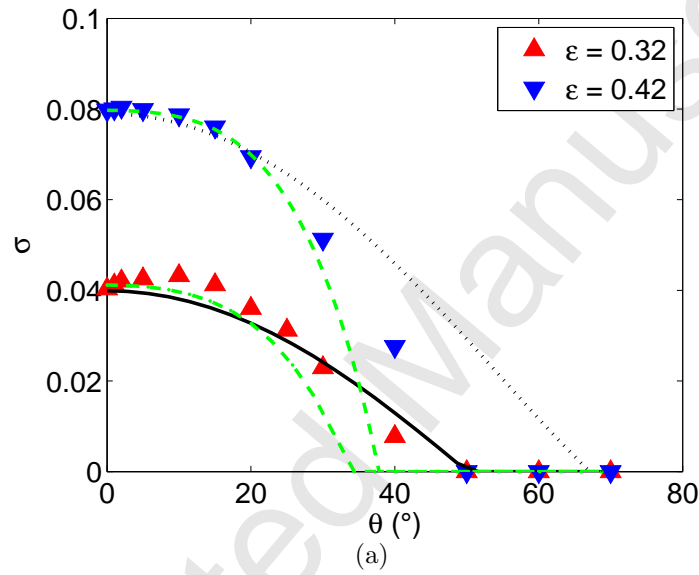


Figure 8: Evolution of the growth rate with the obliquity θ for $E = 1/600$ (fixed angular rate) and two values of the ellipticity $\varepsilon = 0.317$ and $\varepsilon = 0.42$. The dashed dotted line and the dashed line correspond to expression (6), taking into account the values of apparent axes seen from the equatorial plane, whereas the dotted line and the continuous line correspond to expression (3), simply considering the apparent value of the ellipticity seen from the equatorial plane. The coefficient K for viscous corrections is determined at $\theta = 0^\circ$ and then kept constant.

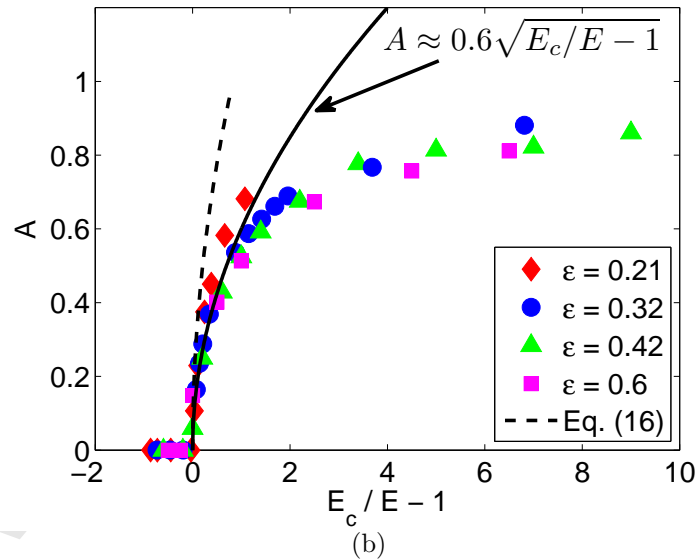
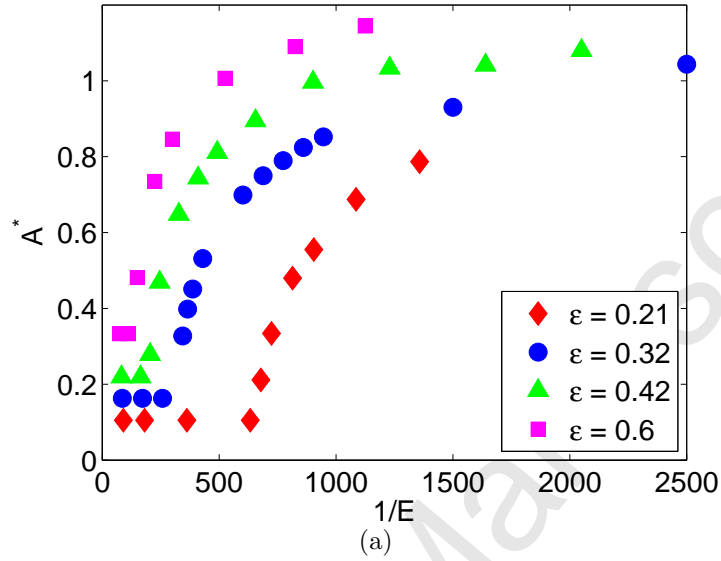


Figure 9: Variation of the saturation amplitude of the flow driven by the elliptical instability depending on the Ekman number, for various values of the ellipticity. (a) Maximum value of the difference between the actual velocity and the theoretical base flow (5). (b) Maximum amplitude of the tidal instability, corresponding to the previous values corrected to take into account recirculation cells: all curves then superimpose when computed as a function of $E_c/E - 1$.

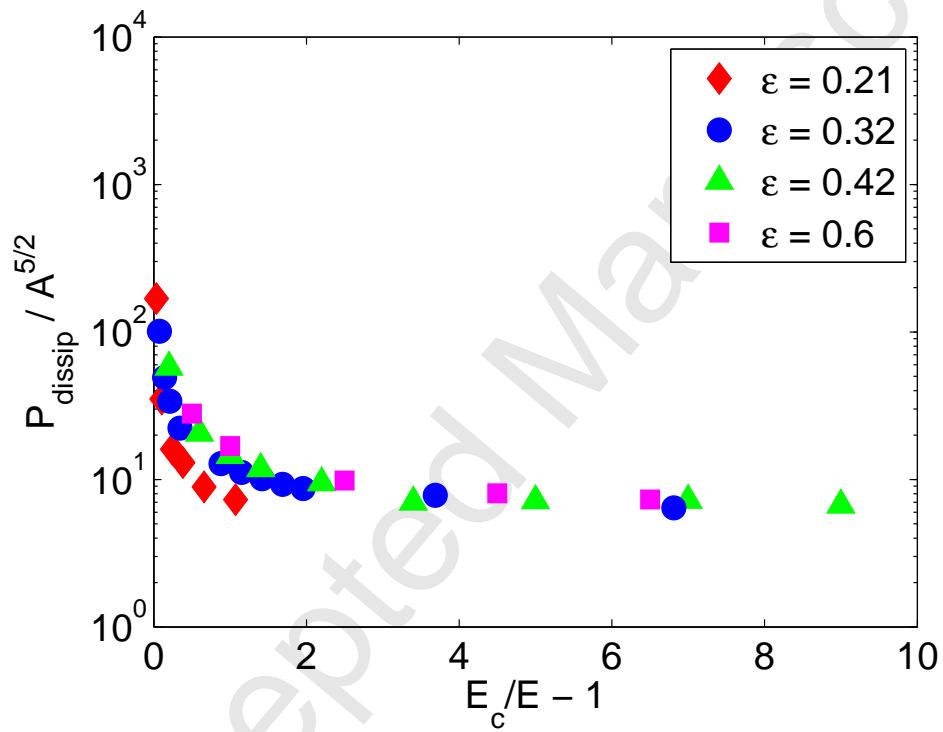


Figure 10: *Viscous dissipation by the tidal instability, as a function of the distance from threshold. The results collapse on a generic law and seem to converge towards a saturation value far from threshold.*